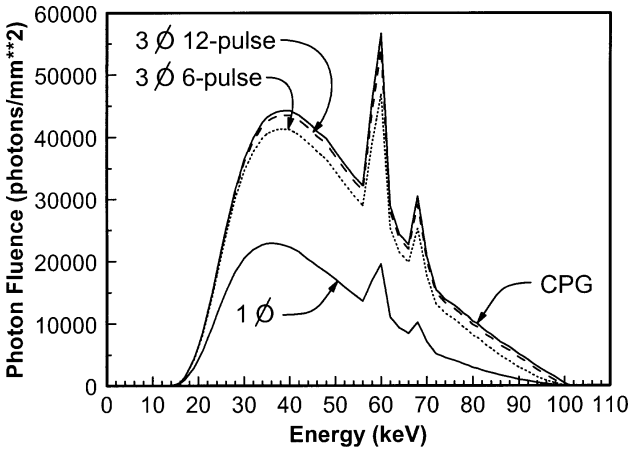

Figure 1.12: The x-ray spectra generated at 100 kVp for four generator technologies are illustrated. In going from single phase to 3-phase-6-pulse to 3-phase-12-pulse to constant-potential generators, both the *quantity* and the *quality* of the x-ray beam increases. There is a negligible difference in the x-ray spectrum between the 3-phase-12-pulse and constant potential generator systems. Modern high-frequency inverter generators produce a spectrum equivalent to 3-phase-12-pulse systems.

are shown at 100 kVp in Figure 1.12. As the ripple decreases from 100% with single-phase generators to 0% with CPG systems, the spectrum becomes slightly higher in average energy, and the output of the x-ray tube (photon fluence, or mR per mAs) increases because x-ray production becomes more efficient at higher energies. The spectra shown in Figure 1.12 were computed with a theoretical model [1] which integrates over the kV-versus-time waveforms produced by the generator technologies listed.

In the late 1980s, high frequency inverter generators were introduced to radiology. Rather than making use of the 60-Hz line frequency supplied by the local power company, high frequency inverter systems convert the primary voltage to DC, and then use a digital oscillator to chop the DC voltage to a high frequency ($\sim$2000 Hz). This voltage waveform is then input to the high voltage transformer, and the high-frequency, high-voltage waveform is rectified, smoothed, and delivered to the x-ray tube. Inverter generators are digitally controlled and by today's standards are less complicated and less expensive than three phase generators, and they produce a low-ripple ($\sim$5%) kV waveform comparable to that of a three-phase twelve-pulse generator.

1.2 X-ray interactions

1.2.1 Interaction mechanisms

X rays (and γ rays) interact with matter in several different types of interactions. Interactions, in general, can result in the local deposition of energy, and in some cases an x ray will exist after the initial interaction in the form of a scattered

x ray, characteristic x rays, or annihilation radiation photons. The types of interactions are the photoelectric effect, Rayleigh scattering, Compton scattering, pair production, and triplet production. The mechanism for each of these interactions is described below.

1.2.1.1 The photoelectric effect

The photoelectric effect was discovered by Albert Einstein in 1905. In the photoelectric interaction, the incident x ray interacts with an electron in the medium. The incident x ray is completely absorbed, and all of its energy is transferred to the electron (Figure 1.13). If the electron is bound to its parent atom with binding energy E_{BE}, and the energy of the incident x ray is given by E_0, the kinetic energy T of the photoelectron is:

$$T = E_0 - E_{BE}. \tag{1.7}$$

If the energy of the incident x ray is less than the binding energy of the electron ($E_0 < E_{BE}$), photoelectric interaction with that electron is energetically unfeasible and will not occur. K-shell electrons are bound more tightly to the atom (higher $|E_{BE}|$) than outer-shell (L shell, etc.) electrons, so if photoelectric interaction is energetically not possible with K-shell electrons, interaction may still occur with an outer-shell electron. When $E_0 = E_{BE}$, then photoelectric interaction is most probable, and the interaction probability decreases with increasing E_0 thereafter. The binding energy, E_{BE}, associated with the K shell is called the K edge, and that of the L shell is called the L edge, and so on. The term *edge* refers to the abrupt jump in the probability of photoelectric interaction once the process becomes energetically possible. The photoelectric effect results in *ionization* of the atom, and a single ion pair (the e^- and the positively charged parent atom) is initially formed. The ejected photoelectron may then proceed to ionize additional atoms in the medium.

Once an electron is liberated from its parent atom, a vacancy in one of the electron shells of the atom exists. A cascade of electron transitions will occur, resulting in the production of characteristic radiation in a manner identical to that described in Section 1.1.2. In that section, atomic electrons were ejected by interaction with bombarding electrons, here the electrons are ejected by photoelectric interaction with an x ray. Either way, the sequence of subsequent events of characteristic x-ray emission is identical, and the reader is referred to Section 1.1.2 and Figure 1.4.

While the post-electron-ejection mechanism of characteristic x-ray production is the same, some practical differences should be mentioned. X rays are produced by electrons striking a high-atomic-number metal target, usually tungsten ($Z = 74$). The characteristic x-ray energies (K_α, K_β, etc.) are therefore quite high. However, x rays used for medical imaging interact first with the patient and then with the x-ray detector. The patient is composed of a medley of elements, but mostly hydrogen ($Z = 1$), carbon ($Z = 6$), nitrogen ($Z = 7$), and oxygen ($Z = 8$), that is, low-atomic-number elements. The K-shell binding energy of oxygen is 0.5 keV, and even that of calcium ($Z = 20$, a constituent of bone) is 4 keV. X rays

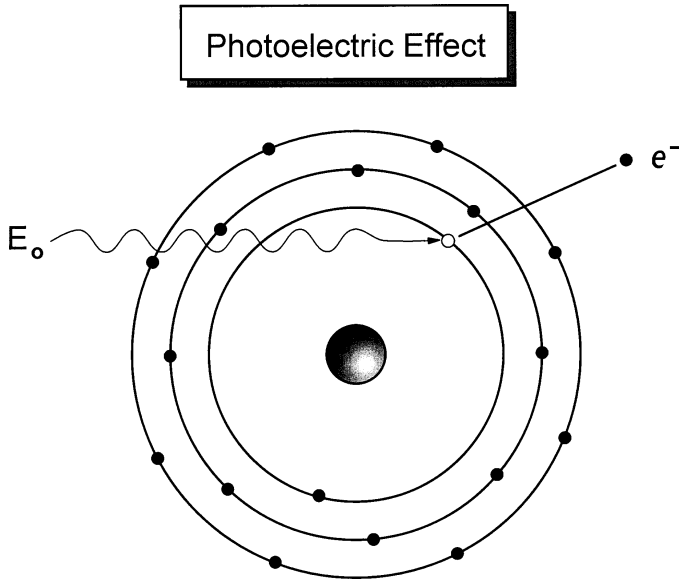

Figure 1.13: In the photoelectric effect, an x ray with energy E_0 is absorbed by an atomic electron, which is ejected from the atom causing ionization. The photoelectron will have kinetic energy equal to $E_0 - E_{\mathrm{BE}}$, where E_{BE} is the binding energy of the electron to the nucleus.

of such low energies do not travel very far before being attenuated. For example, the mean free path of a 1-keV x ray in muscle tissue is about 2.7 μm, less than the dimensions of a typical human cell. Consequently, characteristic x rays that are produced in tissue will be re-absorbed locally in adjacent tissue.

Once the x-ray beam passes through the patient, it will strike the x-ray detector. Typical x-ray detectors are made of CsI, Gd_2O_2S, Y_2TaO_4, etc., with K-shell energies in the 30-keV to 70-keV range. The characteristic x rays produced in the detector itself can be reasonably energetic, and therefore they can propagate finite distances within the detector, or more likely escape the detector completely. This phenomenon will be discussed later.

1.2.1.2 Rayleigh scattering

The mechanism of Rayleigh scattering involves the elastic (coherent) scattering of x rays by atomic electrons (Figure 1.14). The unique feature of Rayleigh scattering is that ionization does *not* occur, and the energy of the scattered x ray is identical to that of the incident x-ray ($E' = E_0$). There is no exchange of energy from the x ray to the medium. However, the scattered x ray experiences a change in its trajectory relative to that of the incident x ray, and this has a deleterious effect in medical imaging, where the detection of scattered x rays is undesirable.

X rays scattered in a three-dimensional coordinate system (real life) require two scattering angles to describe the event. Figure 1.15 shows the geometry of scattering, where the *scattering angle* θ (which ranges from 0 to π) describes the net angular change in photon propagation (looking from the side), and the rotational

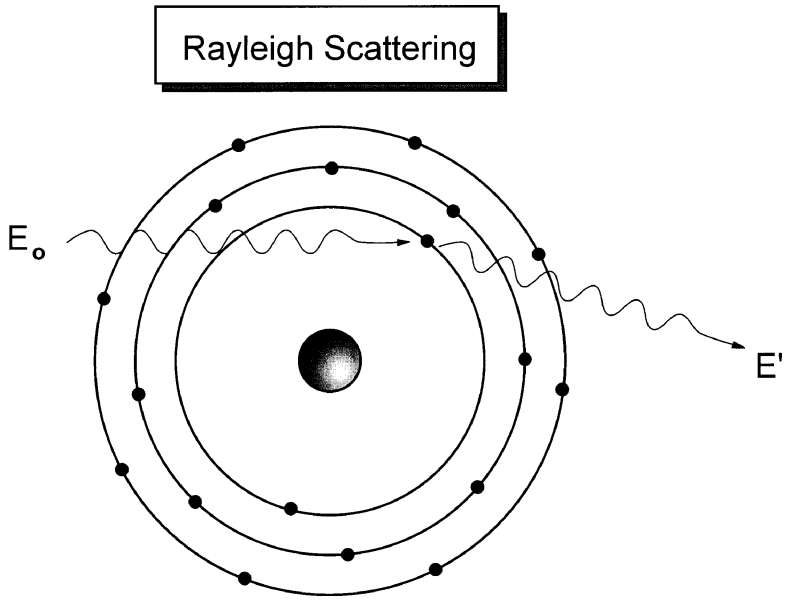

Figure 1.14: In Rayleigh scattering, the incident x ray interacts with the electric field of an orbiting electron and is scattered as a result. The energy of the scattered x ray (E') is equal to the energy of the incident x ray (E_0). No ionization occurs in Rayleigh scattering. Rayleigh scattering is most likely for low-energy x rays and for high-Z absorbers.

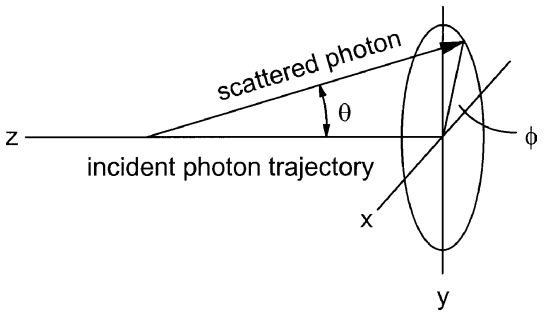

Figure 1.15: The coordinate system for x-ray scattering is illustrated. Two different angles are needed to specify the trajectory of the scattered photon. θ is the scattering angle $(0° - 180°)$. The azimuthal angle (ϕ) spans between $0°$ and $360°$. The scattering angle probability density function, $p(\theta)$, depends on the x-ray energy and scattering mechanism. The probability density function $p(\phi)$ is constant over the $0°$ and $360°$.

angle ϕ (which ranges from 0 to 2π) describes the scattering angle looking down the photon's initial flight path.

Scattering angles θ for Rayleigh scattering in tissue are illustrated in Figure 1.16 for x rays of different energy. The maximum probability at each energy is normalized to 100%. Higher energy x rays (e.g., 60 keV) undergo very small angle scattering (i.e., forward peaked) compared to lower energy x rays (5 keV). This is expected, since the rules of conservation of momentum and energy hold, and the recoil imparted to the atom involved in the interaction must not result in ioniza-

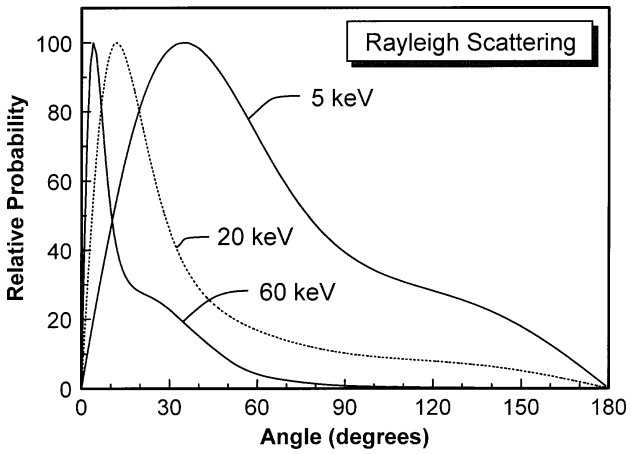

Figure 1.16: The probability density functions for Rayleigh scattering angles are illustrated for three x-ray energies in water. As the x-ray energy increases, forward scattering (small angle scattering) becomes increasingly likely. The PDF at each x-ray energy is normalized to 100%.

tion [2]. Consequently, Rayleigh scattering is more likely for low-energy x rays and high-Z materials.

1.2.1.3 Compton scattering

Compton scattering involves the inelastic (incoherent) scattering of an x-ray photon by an atomic electron (Figures 1.17). Compton scattering typically occurs at higher x-ray energies where the energy of the x-ray photon is much greater than the binding energy of the atomic electron, and therefore the Compton effect is considered to occur with outer-shell, essentially free electrons in the medium. In the Compton effect, an incident x-ray photon of energy E_0 is scattered by the medium, and the products of the interaction include a scattered x-ray photon of energy E', an electron of energy T, and an ionized atom. With Compton scattering, a relationship between the fractional energy loss and the scattering angle θ is observed:

$$\frac{E'}{E_0} = \frac{1}{1+\alpha(1-\cos\theta)}, \tag{1.8}$$

where

$$\alpha = \frac{E_0}{m_0c^2} = \frac{E_0}{511\,\text{keV}},$$

and where m_0c^2 is the rest mass of the electron and is equal to 511 keV. Equation (1.8) is called the Klein-Nishina equation, and qualitatively it implies that the energy of the scattered x-ray photon becomes smaller as the scattering angle increases, and this effect is amplified at higher incident photon energies.

The scattering angle distributions for Compton scattering in tissue are illustrated in Figure 1.18. Low-energy photons are preferentially backscattered,

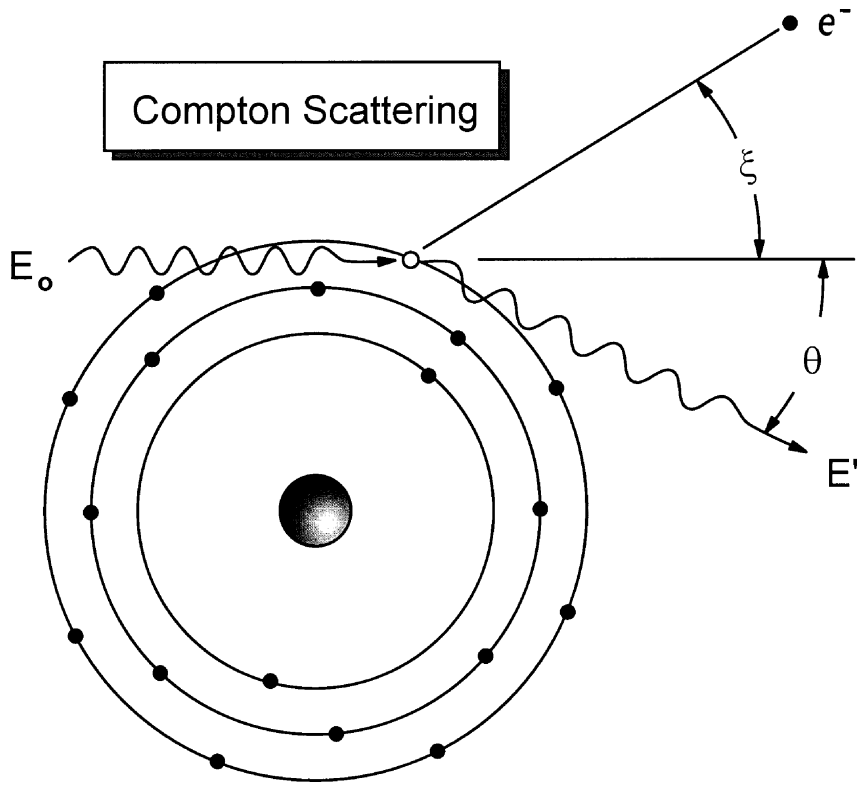

Figure 1.17: In Compton scattering, an incident x ray with energy E_0 interacts with an outer-shell electron. The electron is ejected from the atom, causing ionization. A scattered x-ray photon with energy E' emerges at an angle θ relative to the incident photon's trajectory.

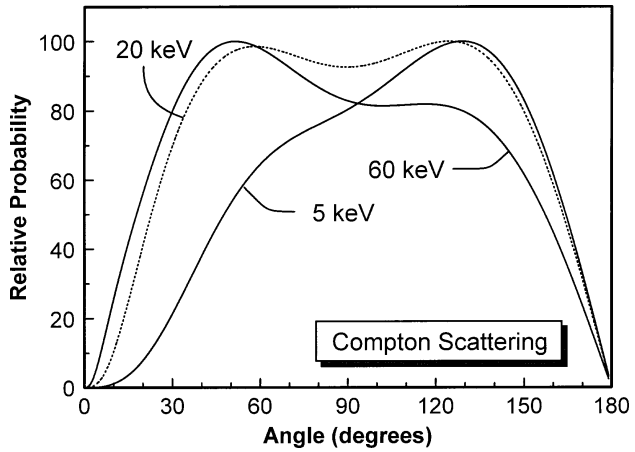

Figure 1.18: The probability density function of Compton scattering as a function of angle is illustrated for three x-ray energies in water. The height of each PDF is normalized to 100%.

whereas higher-energy x rays have a higher probability of forward scattering. At energies well above the diagnostic energy region (e.g., at 5 MeV), Compton scattering is markedly forward peaked.

1.2.1.4 Pair and triplet production

Pair production involves the interaction of an incident x ray with the electric field of the nucleus. Pair production is a classical demonstration of the interchangeability between mass and energy (Figure 1.19). After a pair production interaction, which is only feasible above 1.02 MeV, the incident x ray is completely absorbed and a positron (e^+) and an electron (e^-) are produced (hence the name *pair* production). For an incident x ray of energy E_0 (where $E_0 > 1.02$ MeV),

$$E_0 = 2m_0c^2 + T_+ + T_-, \tag{1.9}$$

where T_+ and T_- are the kinetic energies of the positron and electron, respectively, and m_0 is the rest mass of the electron (and positron). Energy of the incident x ray above 1.02 MeV ($2m_0c^2$) is realized as kinetic energy of the particle pair. It is interesting to note that the atom involved in pair production interaction is not ionized, although charged particles (e^- and e^+) are formed.

Triplet production is similar to pair production, except that the incident x-ray photon interacts with the electric field of an atomic electron instead of the nucleus (Figure 1.20). The atomic electron is ejected from the atom in the process, and it becomes the third particle. Triplet production is energetically feasible only above

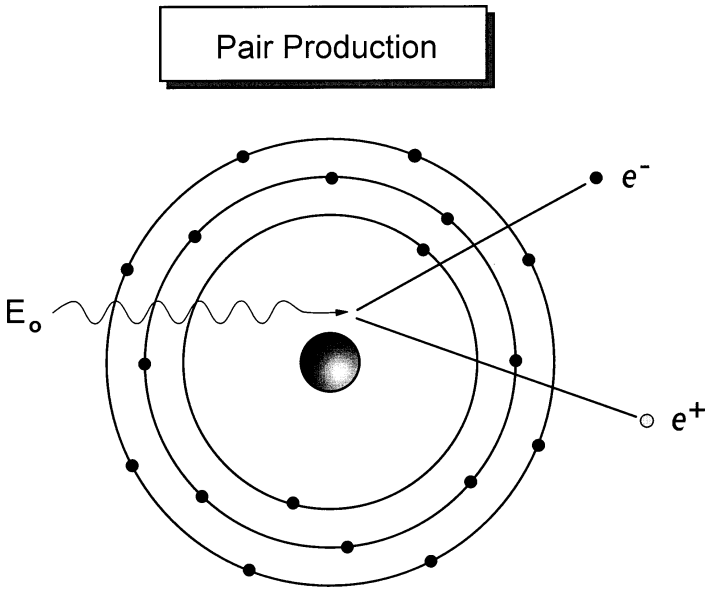

Figure 1.19: Pair production can occur when an incident x ray (with $E_0 > 1.02$ MeV) interacts with the electric field of an atom. A negatron (e^-)–positron (e^+) ion pair is formed in the interaction. Pair production does not occur at diagnostic x-ray energies.

2.04 MeV. Both pair and triplet production result in the formation of energetic electrons, which will cause subsequent ionization events. Once the positron spends its kinetic energy, it will rapidly combine with any available electron, giving rise to *annihilation radiation* as shown in Figure 1.21. The mass of the e^-/e^+ pair disappears, and two 511-keV x-ray photons are produced in nearly opposite directions. If both the e^- and the e^+ have negligible kinetic energy when they annihilate, the trajectories of the two annihilation radiation photons will be exactly opposite to each other. Annihilation radiation photons are used in positron emission tomog-

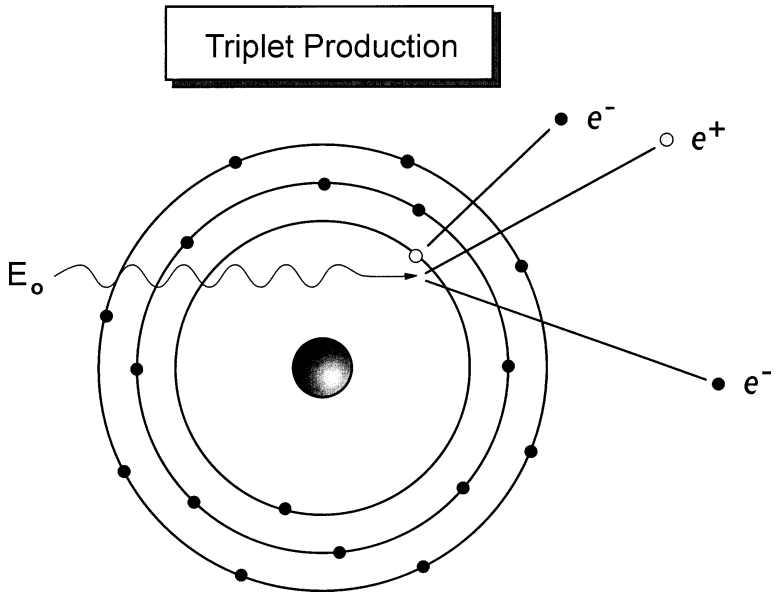

Figure 1.20: Triplet production occurs when an incident x ray ($E_0 > 2.04$ MeV) interacts with the electric field surrounding an orbital electron. The orbital electron is ejected from the parent atom, along with a negatron/positron pair, resulting in three particles being emitted.

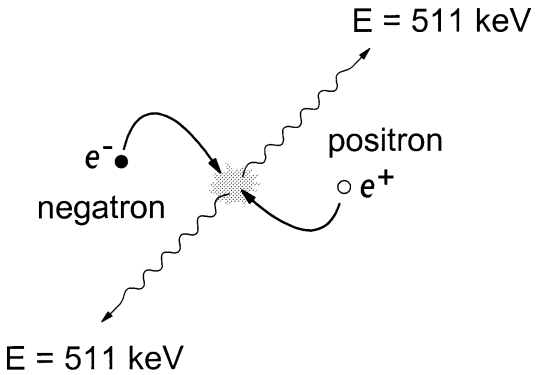

Figure 1.21: The positrons produced in pair and triplet production will lose their kinetic energy by interaction with the medium, and then rapidly interact with any available negative electron (negatron) and *annihilate*, producing two 511-keV photons being emitted in opposite directions. The photons produced are called *annihilation radiation*.

raphy (PET) imaging, however the source of positrons is from radioactive decay, not pair or triplet production. Pair and triplet production take place at energies well above those used in diagnostic radiology, so neither of these processes occur in diagnostic medical imaging.

1.2.2 Attenuation coefficients

1.2.2.1 Linear attenuation coefficient

The interaction mechanisms discussed in the last section combine to produce *attenuation* of the incident x-ray photon beam as it passes through matter. Attenuation is the removal of x-ray photons from the x-ray beam by either absorption or scattering events. If a beam of N x-ray photons is incident upon a thin slab of material of thickness $\mathrm{d}x$ with a probability of interaction μ (Figure 1.22), the reduction of photons from the beam is given by $\mathrm{d}N$, where:

$$\mathrm{d}N = -\mu N \, \mathrm{d}x. \tag{1.10}$$

Rearranging and integrating Eq. (1.10):

$$\int_{N_\mathrm{o}}^{N} \frac{\mathrm{d}N}{N} = -\mu \int_{0}^{t} \mathrm{d}x. \tag{1.11}$$

Solving Eq. (1.11) with subsequent rearrangement results in the Lambert–Beers law:

$$N = N_\mathrm{o} e^{-\mu t}. \tag{1.12}$$

The units of thickness (t) in Eq. (1.12) are typically cm, and so the units of μ must be cm^{-1}; μ is called the *linear attenuation coefficient*. The value of μ represents the probability per centimeter thickness of matter, that an x-ray photon will be attenuated. The linear attenuation coefficient, μ, is the probability of interaction from all interaction mechanisms, and is the sum of the interaction probabilities of all the interaction types:

$$\mu = \tau + \sigma_\mathrm{r} + \sigma + \pi + \gamma, \tag{1.13}$$

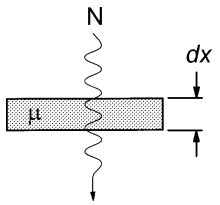

Figure 1.22: For the derivation of the Lambert–Beers Law, an x-ray beam of N photons is incident upon a slab of material with linear attenuation coefficient μ and thickness $\mathrm{d}x$.

where τ is the attenuation coefficient for the photoelectric effect, σ_r is the Rayleigh scatter attenuation coefficient, σ is the Compton attenuation coefficient, π is the pair-production attenuation coefficient, and γ is the triplet attenuation coefficient.

1.2.2.2 Mass attenuation coefficient

The linear attenuation coefficient describes the attenuation properties of a specific material (take water as an example) at a specific x-ray energy. However, the value of the linear attenuation coefficient will depend linearly on the density of the material. For instance, water vapor will have a different μ than liquid water, and frozen water will have yet another value of μ. Since μ changes proportionally with the density of the material, an easy way to compensate for density is to normalize μ by the density (ρ), resulting in the mass attenuation coefficient, (μ/ρ). The mass attenuation coefficients of water vapor, liquid water, and ice are all identical (at a given energy). Since the units of μ are cm^{-1}, and the units of ρ are gm/cm^3, the units of the mass attenuation coefficient are cm^2/gm. When calculating attenuation using the mass attenuation coefficient, the units of thickness logically become the product of the known density ρ and thickness x of the material, ρx, and this product is called the *mass thickness* and has the units gm/cm^2. Thus the Lambert–Beers law becomes:

$$N = N_0 e^{-\left(\frac{\mu}{\rho}\right)\rho x}. \tag{1.14}$$

Just as the total linear attenuation coefficient μ is the sum of the linear attenuation coefficients of the individual interaction types, the total mass attenuation coefficient is the sum of its constituents as well:

$$\left(\frac{\mu}{\rho}\right) = \left(\frac{\tau}{\rho}\right) + \left(\frac{\sigma_r}{\rho}\right) + \left(\frac{\sigma}{\rho}\right) + \left(\frac{\pi}{\rho}\right) + \left(\frac{\gamma}{\rho}\right). \tag{1.15}$$

Attenuation, as calculated by the mass attenuation coefficient (Eq. (1.14)), is useful in describing the propagation of x rays through a material, but it does not tell the complete story in terms of energy deposition. Energy deposition is important both in the calculation of the radiation dose to a patient, and for the calculation of the total signal generated in an x-ray detector.

1.2.2.3 Mass energy transfer coefficient

The mass energy *transfer* coefficient is that fraction of the mass attenuation coefficient which contributes to the production of kinetic energy in charged particles. Photons which escape the interaction site do not contribute to the kinetic energy of charged particles. For the photoelectric effect, at least initially, the total energy of the incident x-ray photon, E_0, is transferred to the photoelectron. Part of this energy is used to overcome the binding energy of the atom (E_{BE}), and the remaining

fraction becomes the kinetic energy T of the photoelectron:

$$\frac{T}{E_0} = \frac{E_0 - E_{\mathrm{BE}}}{E_0}. \tag{1.16}$$

The ionized atom will either emit one or more characteristic x rays (also called *fluorescent* x rays), which will leave the interaction site, or alternatively a series of nonradiative transitions involving Auger electrons will take place, resulting in the complete local deposition of energy through charged particles. The fluorescent yield Y describes the probability of production of characteristic x rays (Y_K is the K-shell fluorescent yield and Y_L is the L-shell yield). The fluorescent yield is virtually zero for $Z < 10$, and Y_K increases with Z thereafter, reaching a value of 0.83 at $Z = 50$, and Y_L is about 0.12 at $Z = 50$. X rays with $E_0 =$ K edge can interact by the photoelectric effect with K-shell electrons, as well as by L-shell (and other shell) electrons. A function P_K describes the fraction of the photoelectric attenuation coefficient that results in K-shell interaction (τ_K/τ), for $E_0 =$ K edge. K-shell characteristic x rays have slightly different energies, depending on the transition levels which occur (e.g., $K_{\alpha 1}$, $K_{\alpha 2}$, $K_{\beta 1}$, $K_{\beta 2}$, etc.), and let the average K-shell fluorescent x-ray energy be designated as $\overline{E}_K$. Similar values (P_L and $\overline{E}_L$) can be defined for the L shell. The photoelectric mass energy transfer coefficient is given by:

$$\frac{\tau_{\mathrm{tr}}}{\rho} = \frac{\tau}{\rho}\left[\frac{E_0 - P_K Y_K \overline{E}_K}{E_0}\right], \quad \text{for } E_0 \geqslant E_{\mathrm{K-edge}}, \tag{1.17a}$$

and:

$$\frac{\tau_{\mathrm{tr}}}{\rho} = \frac{\tau}{\rho}\left[\frac{E_0 - P_L Y_L \overline{E}_L}{E_0}\right], \quad \text{for } E_{\mathrm{K-edge}} > E_0 \geqslant E_{\mathrm{L-edge}}, \tag{1.17b}$$

since the fluorescent yield of the atoms which comprise tissue is negligible, for tissue $(\tau/\rho) = (\tau_{\mathrm{tr}}/\rho)$. This is not the case for x-ray detector materials, however.

Rayleigh scattering does not impart energy to the media, and therefore $(\sigma_{\mathrm{r,tr}}/\rho) = 0$, *always*. For Compton scattering, a large fraction of the incident x-ray energy leaves the site of the interaction in the form of the scattered photon (Eq. (1.8)). If the average kinetic energy imparted to electrons during Compton scattering is E_{k}, then the Compton mass energy transfer coefficient is given by:

$$\frac{\sigma_{\mathrm{tr}}}{\rho} = \frac{\sigma}{\rho}\left[\frac{E_{\mathrm{k}}}{E_{\mathrm{o}}}\right]. \tag{1.18}$$

The mass attenuation coefficients for carbon, iodine, and lead are shown as a function of x-ray energy in Figures 1.23, 1.24, and 1.25, respectively. The mass energy transfer coefficients are also shown where appropriate. The carbon coefficients show no K-edge discontinuities in τ/ρ, because the E_{BE} is below 1 keV. For

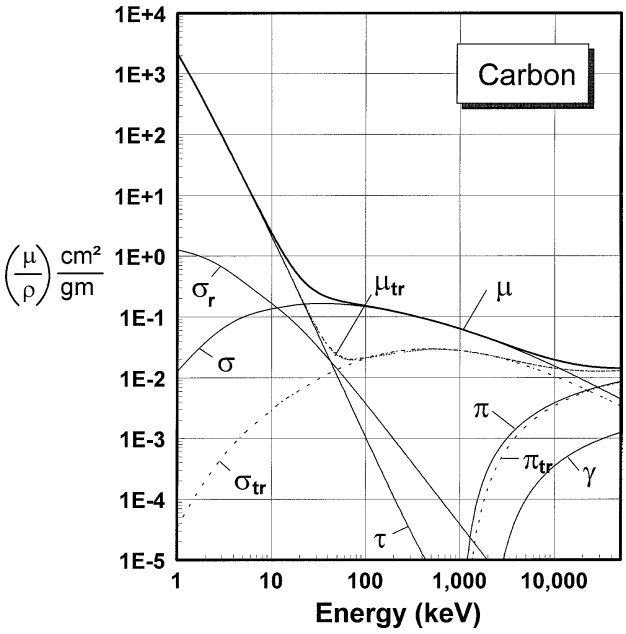

Figure 1.23: The mass attenuation coefficient for carbon is plotted as a function of x-ray energy. See text for definition of symbols.

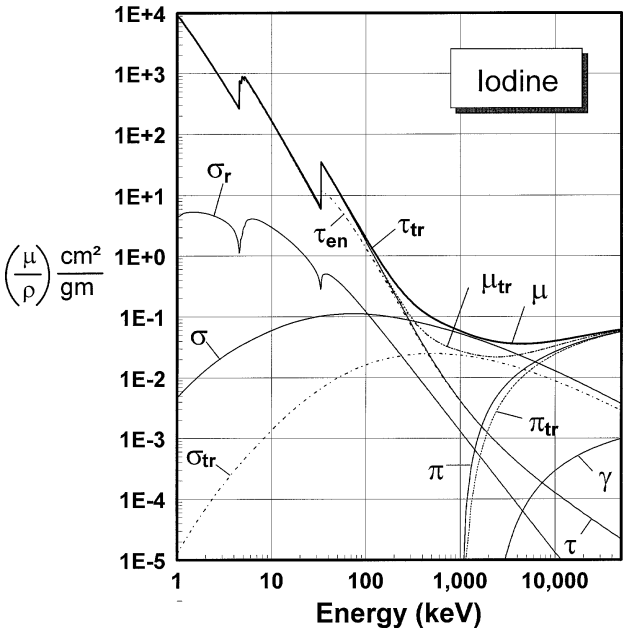

Figure 1.24: The mass attenuation coefficient for iodine is illustrated as a function of x-ray energy. The K edge of iodine (at 33 keV) and the L edge (at 5.2 keV) are apparent.

iodine (Figure 1.24) and lead (Figure 1.25), the L-edge and K-edge discontinuities are seen, and even the M edge is apparent for lead. The K-, L- and M-shell binding energies are plotted as a function of the element (Z) in Figure 1.26. The location

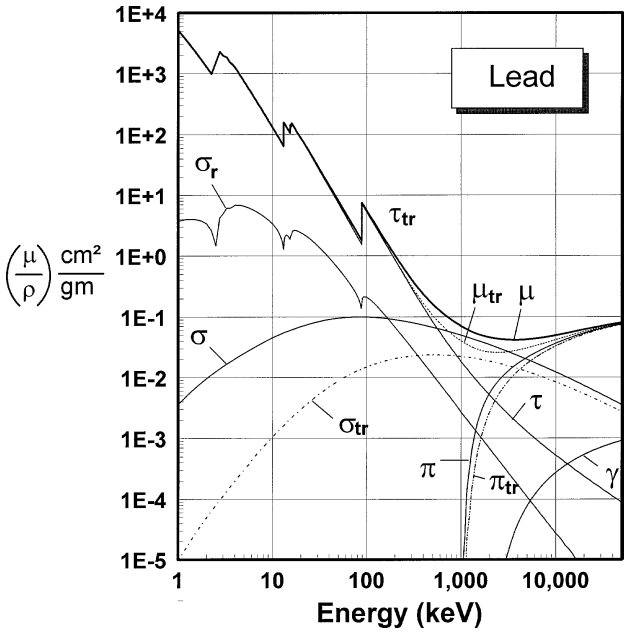

Figure 1.25: The mass attenuation coefficient of lead is shown as a function of x-ray energy. The K edge (88 keV), L edges (around 16 keV), and M edge (∼3 keV) are seen.

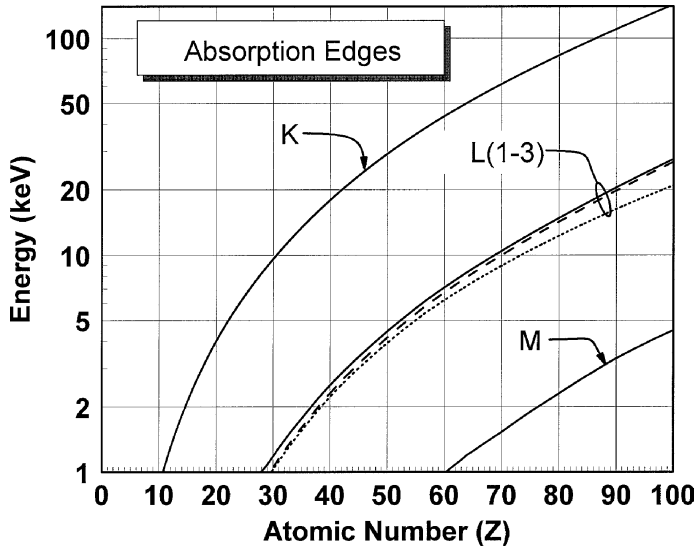

Figure 1.26: The energy of various absorption edges is illustrated as a function of the atomic number of the element. For elements below $Z = 10$ (i.e., tissue), the K edges are below 1 keV. The placement of the K edge of an x-ray detector has a relatively important role to play in the detection properties of the system.

of the K edge, and for higher Z elements the L edge, is important in the design of x-ray detectors for medical imaging, as will be discussed later in this chapter. The atomic number and energy realms in which the photoelectric, Compton, and pair interactions predominate are illustrated in Figure 1.27. The transition line be-

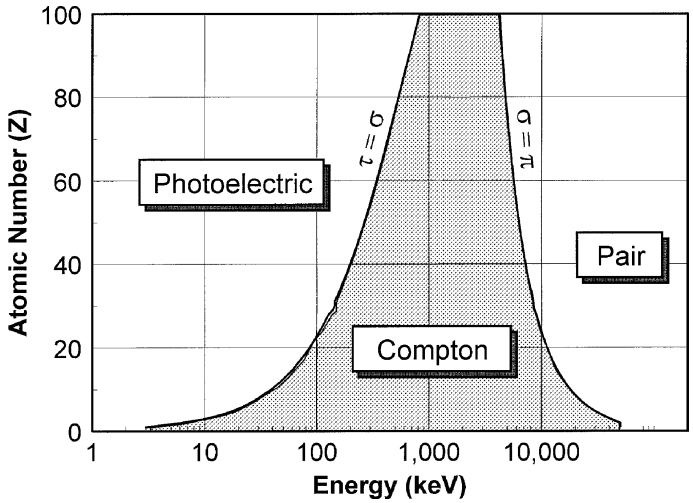

Figure 1.27: The region where each x-ray interaction process is most likely is shown as a function of atomic number and x-ray energy. The transition zones between regions correspond to the two cross sections being equal ($\tau = \sigma$ and $\sigma = \pi$).

tween the photoelectric and Compton zones is defined by $\tau/\rho = \sigma/\rho$, and the line between the Compton and pair production zones is defined by $\sigma/\rho = \pi/\rho$.

Pair and triplet production interactions do not occur at diagnostic x-ray energies, and therefore energy deposition to the patient and detector need not be discussed.

1.2.2.4 Mass energy absorption coefficient

The ratio of the mass energy transfer coefficient, (μ_{tr}/ρ), to the total attenuation coefficient, (μ/ρ), i.e., (μ_{tr}/μ), describes the fraction of the incident x-ray's energy that is transferred to charged particles in the form of kinetic energy. Let the average energy for all charged particles resulting from one interaction be represented as $\overline{E}_k$. As was discussed in Section 1.1.1, energetic electrons can interact with matter and produce bremsstrahlung radiation. The bremsstrahlung radiation that is produced, with an average energy $\overline{E}_r$, will radiate away from the site of the interaction, reducing the locally absorbed energy deposited by charged particles. The mass energy absorption coefficient, (μ_{en}/ρ), takes these radiative losses into account:

$$\left(\frac{\mu_{en}}{\rho}\right) = \left(\frac{\mu_{tr}}{\rho}\right)\left(\frac{\overline{E}_k - \overline{E}_r}{\overline{E}_k}\right). \tag{1.19}$$

For low-Z materials such as tissue, $\overline{E}_r \approx 0$, and thus $(\mu_{en}/\rho) = (\mu_{tr}/\rho)$. Outside of the diagnostic energy range, annihilation radiation losses stemming from pair and triplet production are included in $\overline{E}_r$.

1.2.2.5 Attenuation coefficients for compounds

A compound that is a mixture of N elements will have a mass attenuation coefficient that is the weighted average (by weight) of the elemental mass attenuation coefficients. This is true for (μ_{en}/ρ) and (μ_{tr}/ρ) as well.

$$\left(\frac{\mu}{\rho}\right)_{\text{compound}} = \sum_{i=1}^{N} w_i \left(\frac{\mu}{\rho}\right)_i, \tag{1.20}$$

where w_i is the weight fraction of element i and $(\mu/\rho)_i$ is the mass attenuation coefficient (or mass energy transfer or mass energy absorption coefficients) of element i.

1.2.3 Interaction dependencies

1.2.3.1 Density

Density defines the relationship between the linear and mass attenuation coefficients. The density of each element differs depending on its state and purity, but the published values of the density of each element follow a trend of increasing density at higher Z, as shown in Figure 1.28. The noble gases and the other natural gases (H, O, N, S, Fl, etc.) are low in density, as expected. Interestingly, the rare earths ($Z = 57$ to 72) also are noticeable as a group in the context of density. Removing the gases from the calculation, the relationship between density and Z is approximately $\rho \propto Z^{0.78}$ $(r = 0.76)$.

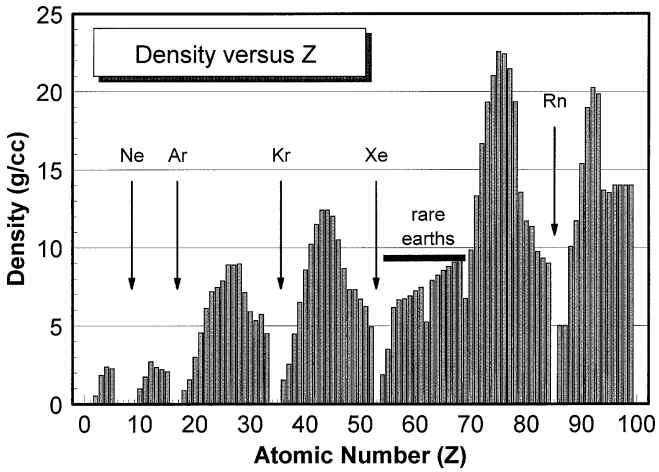

Figure 1.28: Density is shown as a function of atomic number. The low-density noble gases are indicated. The rare-earth elements are seen to disrupt an otherwise repeating pattern. Overall, the density of an element is seen to increase steadily with increasing Z.

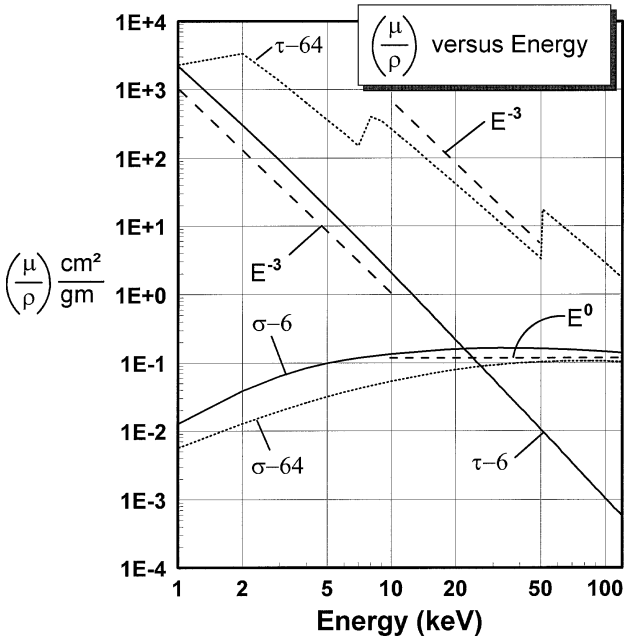

Figure 1.29: The energy dependency of the mass attenuation coefficient for two elements (carbon, $Z = 6$, and gadolinium, $Z = 64$) is illustrated. The photoelectric-effect cross sections for both elements (τ-6 and τ-64) are seen to be parallel to the dash lines indicating an E^{-3} dependency. The Compton scattering cross sections (σ-6 and σ-64) are seen to be essentially constant (proportional to E^0) in the diagnostic energy region from 10 keV to 200 keV.

1.2.3.2 Energy

Figure 1.29 shows the mass attenuation coefficients of carbon ($Z = 6$) and gadolinium ($Z = 64$), for the two prevalent interactions in the diagnostic energy region, the photoelectric (τ) and Compton (σ) effects. Adjacent to the photoelectric attenuation coefficients are dashed lines corresponding to an E^{-3} curve. The E^{-3} curves closely parallel the photoelectric attenuation coefficients for both carbon (τ-6) and gadolinium (τ-64). The Compton-scatter attenuation coefficients are shown, and a line corresponding to E^0 (i.e., no energy dependency) is drawn across the diagnostic energy range from 10 to 100 keV. This E^0 line closely parallels both the carbon (σ-6) and gadolinium (σ-64) Compton coefficients.

1.2.3.3 Atomic number

The mass attenuation coefficients as a function of atomic number (Z) are illustrated in Figure 1.30. Coefficients are shown for 20 keV and 60 keV, as indicated in the figure. Lines corresponding to a Z^4 dependency are shown closely paralleling the photoelectric attenuation coefficients at both energies, although some bowing over occurs at higher Z. The Compton-scattering attenuation coefficients shown in Figure 1.30 are almost horizontal, indicating a Z^0 dependency (i.e., no Z dependency).

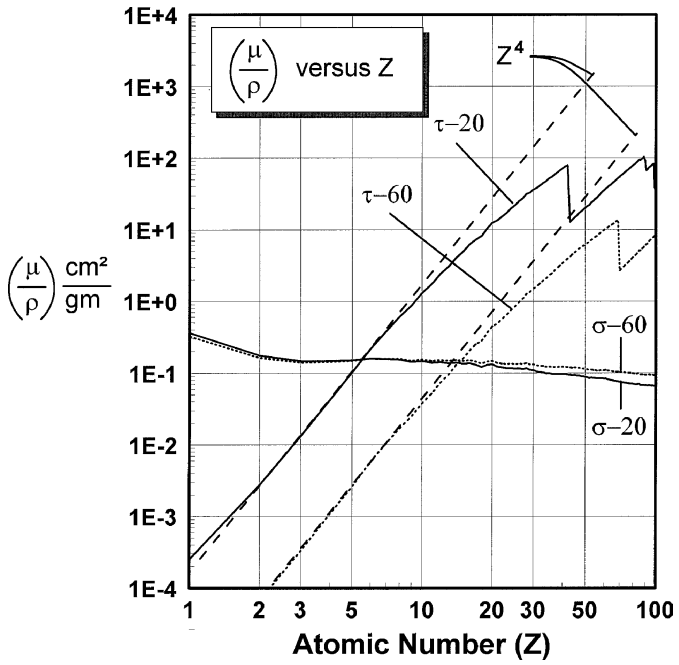

Figure 1.30: The dependency of the *mass attenuation coefficient* on atomic number is illustrated for two x-ray energies (20 keV and 60 keV). The photoelectric-effect cross sections for these two energies (τ-20 and τ-60) are seen to closely parallel dash lines corresponding to a Z^4 dependency. The Compton scattering cross sections at 20 and 60 keV (σ-20 and σ-60) are seen to be essentially constant from helium ($Z = 2$) to Fermium ($Z = 100$). Notice that this plot is for the *mass* attenuation coefficient.

Table 1.2: Attenuation coefficient dependencies

Attenuation Coefficient	Density	Atomic Number	Energy
(τ/ρ)	—	Z^4	$1/E^3$
τ	ρ	Z^3	$1/E^3$
σ	ρ	Z^0 (independent*)	E^0 (independent*)
σ_r	ρ	—	$1/E^{1.2}$

*over the diagnostic x-ray region from 10 to 100 keV.

The linear attenuation coefficient is shown versus the atomic number at 20 keV and 60 keV in Figure 1.31. Because linear attenuation coefficients are significantly effected by the density of the element, there is substantial fluctuation due to the density differences across the elements (recall Figure 1.28). The two dashed lines in Figure 1.31 represent Z^3 dependencies, and there is good agreement between these curves and the data at both x-ray energies. The gases in the periodic table were removed from Figure 1.31. The trends in x-ray attenuation coefficients relevant to diagnostic radiology are summarized below in Table 1.2.

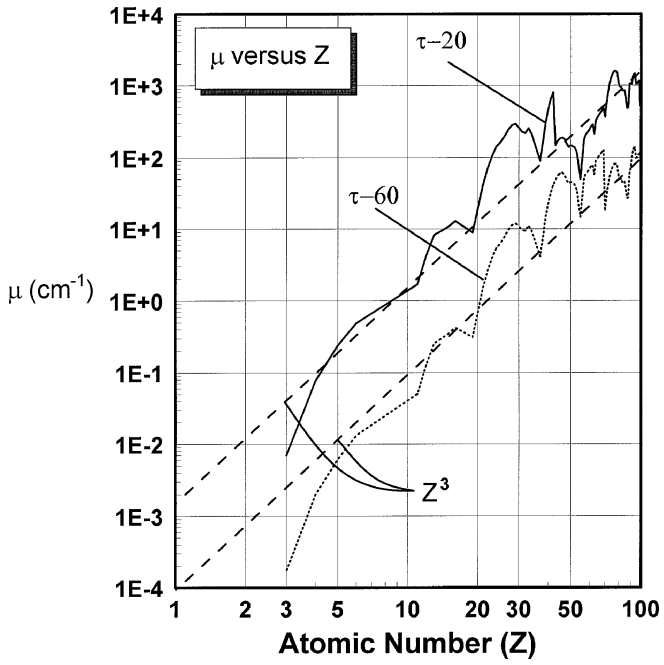

Figure 1.31: The *linear attenuation coefficient* is shown plotted at two different x-ray energies (20 keV and 60 keV) as a function of atomic number. The linear attenuation coefficient, μ, is dependent upon the density of the element and therefore the density-dependent variations (seen in Figure 1.28) are apparent in this figure as well. Gaseous elements were removed from the graph. The linear attenuation coefficient is seen to closely parallel the dashed lines indicating a Z^3 dependency. Note that the Z^3 dependency is for the *linear* attenuation coefficient.

A $\rho \propto Z^{0.78}$ relationship was noted earlier (Figure 1.28), which is essentially the same as $\rho \propto Z^{3/4}$. Dividing the Z^3 dependency of μ by the $Z^{3/4}$ ρ dependency results in the Z^4 dependency of (μ/ρ).

1.2.4 X-ray beam attenuation

In previous sections of this chapter, the mechanisms of x-ray interaction and the energy and atomic number dependencies of the various interaction types were discussed. In this section, the discussion turns to the properties of x-ray beams that are experimentally observable in the radiology department.

1.2.4.1 Good and bad geometry

Attenuation is the removal of photons from the x-ray beam, both by absorption and scattering. To assess attenuation, the x-ray beam that is *not* removed by attenuation is what is actually measured (the primary x-ray beam). It is important that scattered photons not be included in this measurement. Because scattered x rays tend to fly about in all directions near an object being exposed to an x-ray beam, it is important to use a measurement geometry which excludes the measurement of

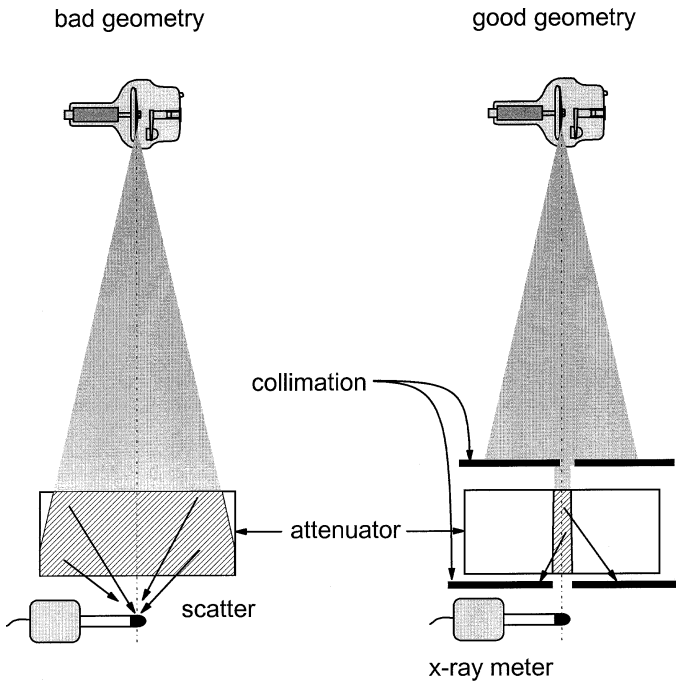

Figure 1.32: The so-called *bad geometry* and *good geometry* for making x-ray attenuation measurements are illustrated. Bad geometry exists whenever the exposure measurement includes an appreciable amount of x-ray scatter from the attenuator. The scatter contribution to the measurement can be reduced by using pre-attenuator collimation to limit the x-ray field and post-attenuator collimation to reduce the chance of scatter reaching the x-ray detector.

scattered x-ray photons, to the extent possible. Figure 1.32 demonstrates *bad* measurement geometry (Figure 1.32(a)), where the placement of the exposure meter near the exit surface of the material will result in a significant contribution of scattered photons to the measured values. *Good* geometry (Figure 1.32(b)) makes use of both pre- and post-material collimators (e.g., sheets of lead), which narrow the x-ray beam substantially. The pre-material collimator limits the area and hence the volume of the material being exposed to radiation, and this will reduce the overall number of scattered photons (specifically, the ratio of scattered to primary photons will be reduced). The post-material collimation serves to limit the scattered photons which are produced in the material so that they have a smaller chance of striking the x-ray exposure meter. Good geometry is also called *narrow-beam* geometry, and bad geometry is also called *broad-beam* geometry.

Another way to reduce the amount of scattered radiation contributing to the measurement is to move the exposure meter away from the scattering material by a reasonable distance. For example, it is a common procedure to measure the attenuation of a number of thin (e.g., 1 mm) aluminum filters (discussed below). For such a measurement, the exposure meter is placed perhaps 100 cm from the x-ray source, and the aluminum filters are placed near at the x-ray tube (typically about 20 cm from the source due to structures near the x-ray tube). Whereas the primary x-ray beam is aimed at the exposure meter and propagates in a straight line

from x-ray source to exposure meter, scattered radiation produced in the filters will in general emerge from the filter with a much wider array of angles. With ample separation between the filter(s) and the exposure meter, the scattered radiation will diverge away from the primary beam and a negligible amount of scatter will be detected in this geometry.

1.2.4.2 Polyenergetic versus monoenergetic attenuation

As Figures 1.24, 1.25, and 1.26 illustrate, attenuation coefficients for a given material are energy dependent. For an x-ray beam composed of a single energy of x-ray photons (a monoenergetic beam), the attenuation of that beam will follow a perfect exponential curve according to the Lambert–Beers law (Eq. (1.12) or (1.14)). The dashed lines on Figure 1.33 shows the attenuation plot for aluminum filters (an x-ray filter is just a thin sheet of metal) at several different x-ray energies. The y axis on Figure 1.33 is logarithmic and the x axis is linear (so the plot is *semi-logarithmic*), and thus an exponential falloff will appear as a perfectly straight line, as the dashed monoenergetic lines indicate. For an x-ray spectrum consisting of many different energies (a polyenergetic spectrum), the attenuation curve (solid line on Figure 1.33) has curvature on the semi-log plot, indicating a slight deviation from exponential falloff. The attenuation, $A(x)$, of a polyenergetic x-ray spectrum,

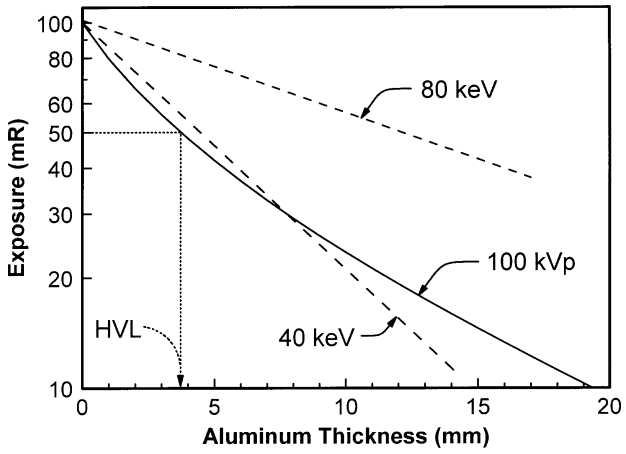

Figure 1.33: Attenuation profiles (exposure as a function of thickness) are shown for aluminum and for three different x-ray beams. The dashed lines are for monoenergetic x-ray beams at 40 keV and 80 keV. Higher-energy x rays are more *penetrating*, so the curve for 80-keV x rays is less steep than the curve for 40-keV x rays. On this semi-logarithmic plot, the attenuation curves for monoenergetic x-ray beams appear as straight lines. For a 100-kVp x-ray spectrum, the attenuation curve demonstrates curvature which is representative of *beam hardening*. The half-value layer (HVL) is the thickness of aluminum required to reduce the exposure of the x-ray beam by 50%. The HVL for the 100-kVp attenuation curve shown is approximately 3.7 mm Al.

$\Phi(E)$, from a sheet of aluminum of thickness x is given by:

$$A(x) = \frac{\int_{E=0}^{E\,\max} \alpha\Phi(E)(\xi(E))^{-1} \exp\left(-\frac{\mu(E)_{\text{al}}}{\rho}\rho x\right) \mathrm{d}E}{\int_{E=0}^{E\,\max} \alpha\Phi(E)(\xi(E))^{-1}\,\mathrm{d}E}, \tag{1.21}$$

where the units of area (α) are mm^2, $\Phi(E)$ is in photons/mm^2 (at each energy E), and the function $\xi^{-1}(E)$ is in the units of mR per (photon/mm^2) (at each energy E). Attenuation is usually measured using an air ionization chamber, which reads out in units of *exposure* (roentgens). The x-ray fluence per unit exposure is given by:

$$\xi(E) = \frac{5.43 \times 10^5}{E\left(\dfrac{\mu_{\text{en}}(E)}{\rho}\right)_{\text{air}}}\quad . \tag{1.22a}$$

When the mass energy absorption coefficient for air, $(\mu_{\text{en}}/\rho)_{\text{air}}$, is in units of cm^2/g, and E is in keV, the units of $\xi(E)$ are photons/mm^2 per mR. $\xi(E)$ describes the photon fluence per unit of exposure, and the inverse function $\xi^{-1}(E)$ describes the exposure per unit of photon fluence. For the energy range from 1 to 150 keV, this can be calculated using:

$$\xi(E) = \left[a + b\sqrt{E}\ln(E) + \frac{c}{E^2}\right]^{-1}, \tag{1.22b}$$

where $a = -5.023290717769674 \times 10^{-06}$, $b = 1.810595449064631 \times 10^{-07}$, $c = 0.008838658459816926$ ($r^2 = 0.9996$), E is in keV, and $\xi(E)$ is in the units of photons/mm^2 per mR. Figure 1.34 shows $\xi(E)$ over the diagnostic energy range. The $\xi^{-1}(E)$ term shows up in Eq. (1.21) because it describes the energy-dependent response of the measuring device, in this case an air-filled ionization chamber.

1.2.4.3 Half-value layer

An air-ionization exposure meter is a device capable of accurately measuring x-ray exposure. Exposure is a term which relates primarily to the x-ray beam intensity or the *beam quantity*. Measuring the x-ray energy spectrum is much more difficult, and requires sophisticated equipment that is only available in a handful of laboratories. Nevertheless, some idea of the spectral distribution (*beam quality*) of the x-ray beam is needed in the field. The x-ray attenuation coefficients are clearly energy dependent (Figure 1.29), and therefore by measuring the attenuation ($A(x)$ in Eq. (1.21)) of a known material (e.g., aluminum), a parameter relating to the x-ray beam energy distribution ($\Phi(E)$) can be assessed. The parameter used to characterize beam quality in field measurements of attenuation is called the *half-value layer* (HVL). The HVL, usually calculated using aluminum in diagnostic radiology, is the thickness of aluminum required to reduce the exposure of the x-ray beam by a factor of 2 (i.e., to 50% of its unattenuated exposure). *Exposure*

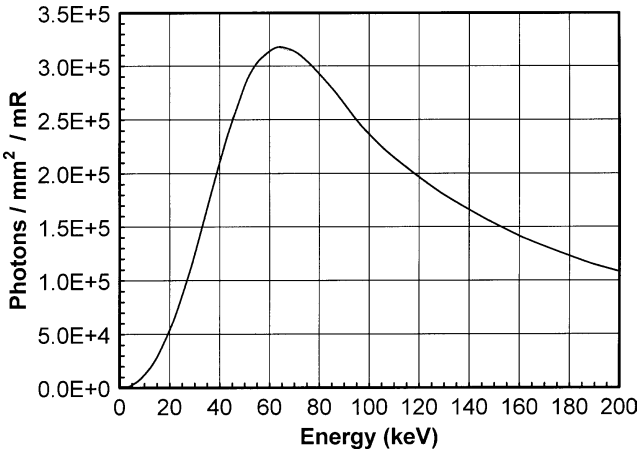

Figure 1.34: The photon fluence (photons/mm^2) per unit exposure (mR) is shown as a function of x-ray energy across the diagnostically relevant energies. X-ray exposure measured in roentgens (or mR) demonstrates energy dependency because the mass energy absorption coefficient for air is energy dependent. This figure illustrates the function $\xi(E)$ as discussed in the text.

is defined in air (only), and therefore the HVL is properly measured only using an air ionization exposure meter; the HVL measured using a solid state x-ray detector system, for example, will be different.

Figure 1.33 illustrates three attenuation curves. For the two dashed lines corresponding to monoenergetic x-ray beams, the slope of the line (when corrected for units) is the linear attenuation coefficient. The relationship HVL $= \ln(2)/\mu$ can be easily derived. The HVL is shown graphically for the 100-kVp polychromatic x-ray beam shown in Figure 1.33, and is approximately 3.7 mm Al. For higher energy beams the HVL will increase, and for lower kVp beams the HVL will decrease.

1.2.4.4 Beam hardening

Because the polychromatic attenuation profile in Figure 1.33 shows curvature, the slope (proportional to μ) changes depending upon the amount of aluminum filtration present in the beam. This is evidence of *beam hardening*. A *hard* x-ray beam is one with higher energy, a *soft* x-ray beam is a lower-energy beam. Beam hardening is a process whereby the average energy of the x-ray beam increases as that beam passes through increasing thicknesses of an absorber. Beam hardening occurs because as a polyenergetic x-ray beam passes through an absorber, the lower-energy x-ray photons are attenuated more (per unit thickness) than are the higher-energy photons. This is a direct consequence of the energy-dependence of attenuation coefficients, which are higher at lower energies (see for example Figure 1.24).

To demonstrate beam hardening more directly, Figure 1.35 shows the same 100-kVp x-ray spectrum passed through different thicknesses of aluminum. As the thickness of the aluminum increases from 0 mm to 30 mm, two trends are observed:

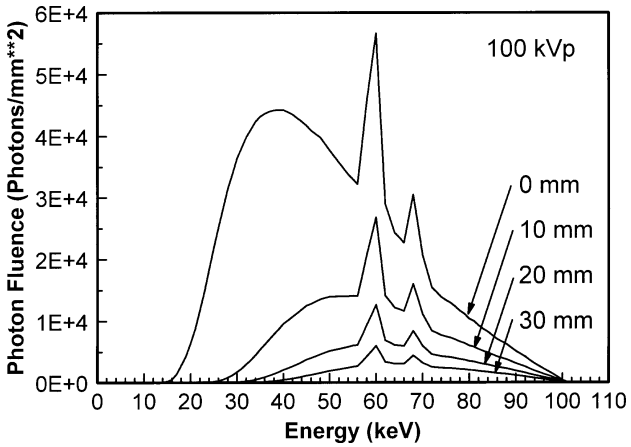

Figure 1.35: X-ray spectra corresponding to different amounts of aluminum filtration are shown. With increasing aluminum filtration thickness (indicated), the area of the x-ray spectra shown is substantially reduced (fewer x-ray photons). In addition, a gradual shift towards higher energies in the more attenuated spectra is observed. The shift in average or effective beam energy with increasing filtration thickness is called *beam hardening*.

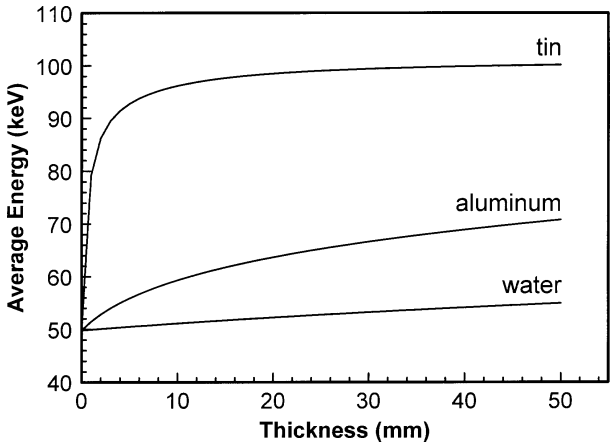

Figure 1.36: The average x-ray energy in a 100-kVp x-ray spectrum is illustrated as a function of thickness for three different attenuators. Fifty millimeters of water produces only a modest increase in average x-ray energy, whereas 50 mm of aluminum causes a more noticeable increase in average energy. Because of the high atomic number and density of tin ($Z = 50$, $\rho = 7.3$ g/cm^3), it has a profound beam-hardening effect.

(1) the number (quantity) of x rays decreases at each energy, and (2) the lower-energy photon fluence decreases proportionately more than the higher-energy fluence, that is, the beam becomes harder. The average energy of a 100-kVp x-ray beam was calculated as the beam was passed through different thicknesses of water, aluminum, and tin, as shown in Figure 1.36. The increase in the average energy of the x-ray spectrum as a function of the thickness of absorber is another direct way to illustrate beam hardening. Higher Z absorbers ($Z_{Al} = 13$, $Z_{Sn} = 50$) cause

more beam hardening per unit thickness, partially because of their higher density, and partially because of the Z^3/E^3 x-ray interaction dependency.

1.3 X-ray spectra

The physics behind the production of x rays was discussed in Section 1.1. In this section, some practical issues and applications of general radiographic and mammographic x-ray spectra are discussed. The conventional notation for *photon fluence* (e.g., photons/mm^2) at a given energy E is $\Phi(E)$. The corresponding *energy fluence* (e.g., joules/mm^2 or $\Phi(E) \times E$) is $\Psi(E)$.

1.3.1 Diagnostic x-ray spectra

1.3.1.1 X-ray filtration

X-ray spectra used for general diagnostic radiology are generally produced with tungsten target x-ray tubes at kVp's ranging between 40 kVp and 150 kVp. Even at the same kVp, each x-ray system will produce slightly different x-ray spectra. The factors which cause the variation between spectra from different x-ray systems include the calibration of the system, the generator waveform (discussed in Section 1.1.2.3), the anode angle, and the amount of filtration which is present both inside and outside the x-ray tube and its housing. The x rays produced at the x-ray tube target must pass through the glass or metal envelope of the x-ray tube, a thin layer of oil, the plastic x-ray tube port (in the housing), a mirror in some cases, in addition to aluminum or other filters which are intentionally placed in the beam (Figure 1.37). The *inherent filtration* of an x-ray tube refers to the objects in the beam path that are a part of the x-ray tube, its housing, and collimator. *Added filtration* refers to the sheets of metal (usually aluminum, but sometimes copper, erbium, or other materials) placed intentionally in the beam. The *total filtration* is the sum of the inherent and added filtration, expressed in terms of aluminum equivalence. The glass x-ray tube envelope is comprised mostly of silicon ($Z = 14$), very similar to aluminum ($Z = 13$), which makes aluminum equivalence possible.

The amount of beam filtration affects the x-ray spectra in a profound way. Because x-ray spectra at the same kVp differ, when referring to beam quality it is common to state both the kVp and the half-value layer (HVL). In the past, a term called the *homogeneity coefficient* was advocated as an additional descriptor of beam quality. The homogeneity coefficient is the ratio of the first HVL to the second HVL.

1.3.1.2 An x-ray spectral model

Many investigators have developed algorithms or models to predict the shape of an x-ray spectrum given the kVp and other parameters of the x-ray beam. A complete review of spectral models will be avoided here, but recent comparisons between various models have been made [3]. Kramer's model [4] for the bremsstrahlung spectrum was one of the first spectral models (1923), and in essence is described by Eq. (1.4). The spectral model of Tucker, Barnes, and

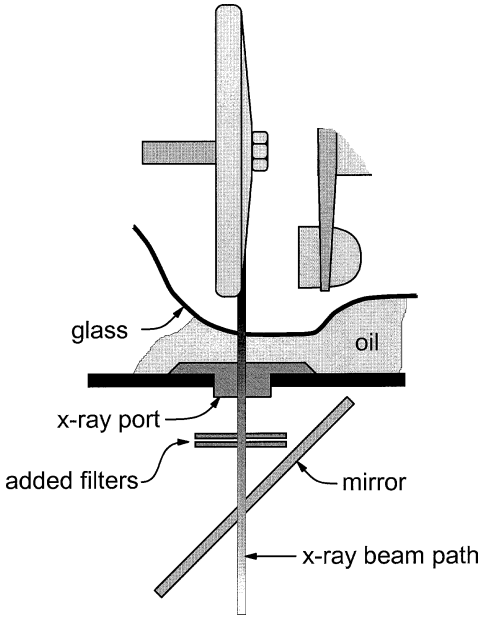

Figure 1.37: A close-up diagram of the components in an x-ray tube which an x-ray beam must pass through is shown. After production and some self filtration in the tungsten anode, x rays must pass through the glass (or sometimes metal) x-ray tube housing, a layer of oil which surrounds the x-ray tube insert for thermal and electrical insulation, the x-ray tube port, and other structures in the beam such as the mirror which is present in the collimation assembly of most clinical x-ray systems. These necessary structures in the x-ray beam constitute the *inherent* filtration. Most clinical x-ray systems have *added* filtration (usually sheets of aluminum) as well.

Chakraborty [5] is commonly used today. This model is semi-empirical, that is its derivation uses principles from basic physics coupled with phenomenological data. The Tucker, Barnes, and Chakraborty model produces high (energy) resolution x-ray spectra with excellent adherence to measured data.

Measured x-ray spectra remain the gold standard of computer-generated models. Boone and Seibert [1] recently developed a completely empirical model, based on the physically measured x-ray spectra published by Thomas Fewell [6]. Because of the accuracy and simplicity of the model (and the familiarity of this author with it), it will be briefly described. The *t*ungsten *a*node *s*pectral *m*odel using *i*nterpolating *p*olynomials (TASMIP) is based on 11 spectra measured photon-by-photon by x-ray spectroscopy. Figure 1.38 illustrates the measured spectra, where each spectrum has been normalized to a tube current of 1.0 mAs. At each energy interval, the photon fluence increases as the kVp is increased, and of course the maximum energy in each spectrum increases with increasing kVp as well. Characteristic x-ray production (the K_α and K_β lines of the tungsten anode) is not seen in spectra below 70 kVp, as described in Section 1.1.2. The vertical lines marked A, B and C in Figure 1.38(a) highlight the 40, 60 and 80 keV energy intervals. The data points where these vertical dashed lines intersect the measured spectra on Fig-

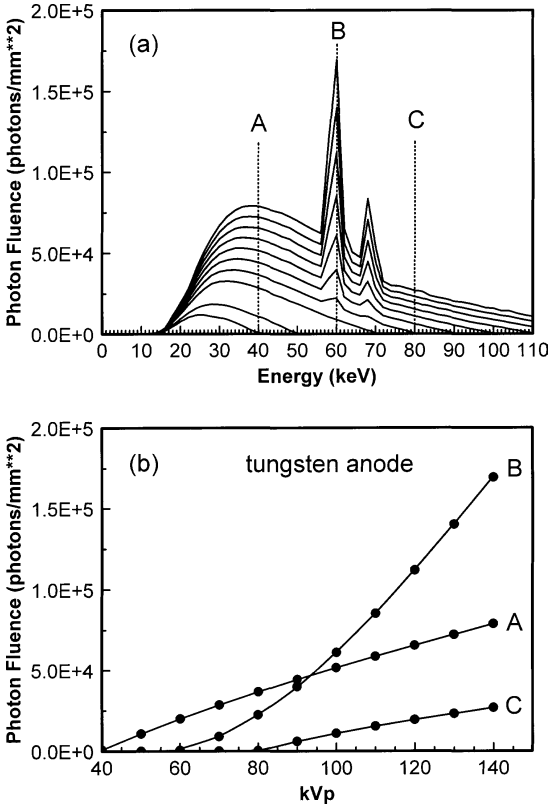

Figure 1.38: The basis of the TASMIP x-ray spectral model is shown. (a) Measured x-ray spectra reported by Fewell are shown. Where each spectra intersects a vertical line (e.g., the dotted line marked "A"), the photon fluence at that energy (e.g., 40 keV) is seen. The photon-fluence values where the dotted line "A" intersects the x-ray spectra are plotted as a function of kVp in (b). A smooth polynomial fit between the measured data points allows the calculation of the 40-keV x-ray photon fluence as a function of kVp. A similar procedure is carried out at all x-ray energies (at 1-keV intervals, the vertical lines marked "B" and "C" illustrate two other examples) to accurately compute an x-ray spectrum at any arbitrary kVp.

ure 1.38(a) are plotted as a function of the kVp as the solid circles in Figure 1.38(b). The lines interpolating the data in Figure 1.38(b) are polynomial fit results to the measured points. It is clear from the figure that an excellent fit is achieved due to the relatively smooth behavior of the data, and this fit was achieved using a maximum of 4 polynomial coefficients. The accuracy of the polynomial fit shown for 3 energies (40, 60, and 80 keV) in Figure 1.38(b) is representative of that for all other energies, and is the accuracy of the TASMIP spectral model.

The TASMIP model uses polynomial interpolation at each energy in the x-ray spectrum, from 0 keV to 140 keV in 1 keV steps. Using predetermined polynomial-fit coefficients ($a_i[E]$) derived from Fewell's measured data, an x-ray spectrum $\Phi(E)$ at any kVp can be computed:

$$\begin{aligned} &\Phi(E) = a_0[E] + a_1[E]\mathrm{kVp} + a_2[E]\mathrm{kVp}^2 + a_3[E]\mathrm{kVp}^3; && \text{for } E \leqslant \mathrm{kVp} \\ &\Phi(E) = 0; && \text{for } E > \mathrm{kVp}. \end{aligned} \tag{1.23}$$

A matrix of 564 coefficients (141 energies × 4 coefficients per energy) provides all the data necessary to reconstruct spectra at any kVp from 30 to 140 kVp. The TASMIP model is accurate both in terms of quality (shape of spectrum) and quantity (mR per mAs per kVp). Because the measured spectra that are the basis of the TASMIP model were from a constant potential generator, integration of the CPG spectra over a sinusoidally fluctuating kV allows the model to be adapted to produce spectra with arbitrary amounts of generator ripple (0%–100%).

The TASMIP model produces x-ray spectra for a naked tube: one with no added filtration. Several representative x-ray spectra generated with the TASMIP model are included in Table 1.3. Using published values for attenuation coefficients of the elements [7], arbitrary filtration can be applied to the naked spectra using the energy-dependent Lambert–Beers law. The coefficients and the source code for the TASMIP model can be downloaded via FTP from ftp://ftp.aip.org/epaps/medical_phys/E-MPHYA-24-1661/. All of the tungsten diagnostic x-ray spectra plotted in this chapter make use of the TASMIP model.

1.3.1.3 Effective versus average energy

It is often convenient to make estimates about the penetration capabilities or dose of an x-ray beam by assuming it is monoenergetic with some average energy. The *average energy* of an x-ray spectrum is calculated as the simple energy-weighted average:

$$\overline{E}_{\text{ave}} = \frac{\int_{E=0}^{E\,\text{max}} E\,\Phi(E)\,\mathrm{d}E}{\int_{E=0}^{E\,\text{max}} \Phi(E)\,\mathrm{d}E}. \tag{1.24}$$

The average energy is a useful measure of a spectrum that is already known (i.e., to compute the average energy, $\Phi(E)$ needs to be known). In many experimental situations, however this is not the case. Usually, only attenuation data are available. In this situation, the *effective energy* can be estimated. The effective energy is assessed as follows: The attenuation factor, N/N_{o} (Eq. (1.14)) of a small thickness (t) of aluminum is measured. The monoenergetic Lambert–Beers equation (Eq. (1.14)) is then used (even though a polyenergetic beam was evaluated), and knowing N/N_{o} and the aluminum thickness and density, the (μ/ρ) of aluminum is calculated. The value of (μ/ρ) is then compared to a table for aluminum of (μ/ρ) versus energy (Table 1.4 is provided below for this). Using log-log interpolation, the effective energy is calculated as that energy which matches the measured (μ/ρ). Because of beam hardening, if the effective energy of the unattenuated x-ray beam is of interest, the thickness of aluminum used for assessing attenuation should be small, e.g., 0.1 or 0.5 mm.

The average energy of various x-ray spectra is plotted in Figure 1.39. Added aluminum filtration has an appreciable effect on the average energy of the beam. For example, a 140-kVp beam with 0 mm added Al has the same average energy as a 110-kVp beam with 2 mm of added Al. The line which defines $E = 1/2$ kVp is also illustrated in Figure 1.39. For the curve corresponding to 2 mm of added

Table 1.3(a): X-ray spectra for kV 30 through 80. These spectra were generated by the TASMIP model reported in [1]. The spectra are representative of a tungsten anode x-ray tube with a 5% kV ripple (inverter generator), and with no added filtration to the x-ray tube. Each spectrum is normalized to 1.0 mR, and the tabulated numbers refer to the number of photons per mm^2 at each energy bin. Each energy bin has a width of 2 keV, and the number reported is at the center of that bin (e.g., 22.5 includes all 22 and 23 keV photons)

E (keV)	30 kV	40 kV	50 kV	60 kV	70 kV	80 kV
12.5	1.4041e + 2	9.2699e + 1	6.4350e + 1	4.8250e + 1	3.8670e + 1	3.2733e + 1
14.5	1.2540e + 3	6.9331e + 2	4.4926e + 2	3.2983e + 2	2.6301e + 2	2.2024e + 2
16.5	4.0961e + 3	2.4179e + 3	1.6510e + 3	1.2620e + 3	1.0359e + 3	8.8286e + 2
18.5	7.8961e + 3	5.0731e + 3	3.6755e + 3	2.9326e + 3	2.4833e + 3	2.1635e + 3
20.5	1.1621e + 4	7.8266e + 3	5.7929e + 3	4.6650e + 3	3.9624e + 3	3.4521e + 3
22.5	1.3420e + 4	9.9301e + 3	7.7221e + 3	6.4064e + 3	5.5474e + 3	4.8958e + 3
24.5	1.2047e + 4	1.0912e + 4	9.1883e + 3	7.9342e + 3	7.0305e + 3	6.2977e + 3
26.5	7.6392e + 3	1.0562e + 4	9.9433e + 3	9.0129e + 3	8.1916e + 3	7.4466e + 3
28.5	2.5339e + 3	9.5575e + 3	1.0162e + 4	9.6494e + 3	8.9812e + 3	8.2810e + 3
30.5	7.5966e + 2	8.7827e + 3	9.9344e + 3	9.7213e + 3	9.2436e + 3	8.6729e + 3
32.5	—	7.4717e + 3	9.4052e + 3	9.5486e + 3	9.2665e + 3	8.8181e + 3
34.5	—	5.5920e + 3	8.5233e + 3	9.1262e + 3	9.0946e + 3	8.8008e + 3
36.5	—	3.3908e + 3	7.4825e + 3	8.5701e + 3	8.7775e + 3	8.6199e + 3
38.5	—	1.2051e + 3	6.3505e + 3	7.9123e + 3	8.3658e + 3	8.3542e + 3
40.5	—	1.9783e + 2	5.4170e + 3	7.2392e + 3	7.8754e + 3	8.0009e + 3
42.5	—	—	4.3420e + 3	6.4903e + 3	7.3223e + 3	7.5807e + 3
44.5	—	—	3.0938e + 3	5.6070e + 3	6.6620e + 3	7.0749e + 3
46.5	—	—	1.8524e + 3	4.8788e + 3	6.1522e + 3	6.6695e + 3